

# Observation of Superradiant Bursts in a Cascaded Quantum System

Christian Liedl<sup>1</sup>, Felix Tebbenjohanns, Constanze Bach, Sebastian Pucher<sup>1,\*</sup>,  
Arno Rauschenbeutel<sup>1</sup>, and Philipp Schneeweiss<sup>1,†</sup>

*Department of Physics, Humboldt-Universität zu Berlin, 10099 Berlin, Germany*

 (Received 5 December 2022; revised 26 June 2023; accepted 2 January 2024; published 16 February 2024)

We experimentally investigate the collective radiative decay of a fully inverted ensemble of two-level atoms for a chiral, i.e., propagation direction-dependent light-matter coupling. Despite a fundamentally different interaction Hamiltonian which has a reduced symmetry compared to the standard Dicke case of superradiance, we do observe a superradiant burst of light. The burst occurs above a threshold number of atoms, and its peak power scales faster with the number of atoms than in the case of free-space Dicke superradiance. We measure the first-order coherence of the burst and experimentally distinguish two regimes, one dominated by the coherence induced during the excitation process and the other governed by vacuum fluctuations. Our results shed light on the collective radiative dynamics of cascaded quantum many-body systems, i.e., systems in which each quantum emitter is only driven by light radiated by emitters that are upstream in the cascade. Our findings may turn out useful for generating multiphoton Fock states as a resource for quantum technologies.

DOI: [10.1103/PhysRevX.14.011020](https://doi.org/10.1103/PhysRevX.14.011020)

Subject Areas: Atomic and Molecular Physics,  
Quantum Physics

## I. INTRODUCTION

When a single quantum emitter interacts with a propagating light field, one usually assumes that the emitter–light coupling strength is independent of the sense of propagation of the light, forward or backward [1]. However, under certain circumstances, this symmetry can be broken, rendering the interaction between the emitter and the field mode propagation direction dependent or “chiral” [2]. This chiral coupling lends itself to the implementation of spin-controlled nonreciprocal devices [3] and is a powerful resource in quantum information [4,5]. When more than one quantum emitter is chirally coupled to a common optical mode, this realizes a so-called cascaded quantum system [6,7]. There, each quantum emitter is only driven by light radiated by emitters that are upstream in the cascade. In other words, there is only one direction in which information about each subsystem can propagate through the ensemble.

One of the hallmark collective effects of “symmetric” quantum optics is Dicke superradiance [8,9], where an

ensemble of initially excited atoms emits light in a short, so-called superradiant burst into an optical mode. The burst is characterized by an initial increase of the emitted optical power, which is due to a spontaneous synchronization of the initially independent atomic dipoles. The study of such superradiant emission in spatially extended atomic ensembles has seen a revival in recent years, driven by an increasing level of experimental control [10–16] and theoretical efforts to understand the intricacies of such many-body quantum systems [17–24]. In his seminal work, Dicke analyzed an atomic ensemble which featured particle exchange symmetry; i.e., the system Hamiltonian is invariant under the exchange of two participating atoms [8,25]. Because of this symmetry, the ensemble remains in the subspace of so-called symmetric Dicke states, which makes the problem analytically solvable even for a large number of atoms [9]. In contrast, the interaction Hamiltonian of a cascaded quantum system does not feature particle exchange symmetry [26–28]. This implies, e.g., that the first atom in the cascade is completely independent of the rest of the ensemble, while the dynamics of the last atom depends on all other atoms. Recently, it has been theoretically predicted that superradiant bursts occur even for perfectly unidirectional coupling [29]. This dynamics has, however, not been observed experimentally.

Here, we observe a superradiant burst emission by about 1000 cesium atoms that are chirally coupled to a nanophotonic waveguide. The atomic ensemble extends over thousands of optical wavelengths and features waveguide-mediated long-range interactions [30]. The atoms are

\*Present address: Max-Planck-Institut für Quantenoptik, Hans-Kopfermann-Straße 1, 85748 Garching, Germany.

†philipp.schneeweiss@hu-berlin.de

*Published by the American Physical Society under the terms of the Creative Commons Attribution 4.0 International license. Further distribution of this work must maintain attribution to the author(s) and the published article's title, journal citation, and DOI.*

excited through the waveguide by means of a short resonant optical pulse. Following this excitation, the ensemble emits a burst of light into the waveguide if the number of atoms exceeds a threshold value. Interestingly, we find that the peak power of this burst scales faster with the number of atoms than in the case of Dicke superradiance in free space. We show that, because of the initial coherence that is present in the atomic ensemble after excitation, the superradiant bursts are coherent with respect to the excitation laser field for a wide range of excitation pulse areas. However, when the excitation pulse area is chosen such that the ensemble is prepared close to full inversion, the coherence of the superradiant burst with respect to the excitation laser field is lost. This shows that the burst emitted by a fully inverted ensemble is induced by vacuum fluctuations. Consequently, it exhibits a vanishing expectation value of the electric field, meaning that its phase is undefined. Still, even then, we find that the field at the beginning of the burst is coherent with the field at later times, indicating that the vacuum-induced burst is primarily emitted into a single temporal mode. Finally, we present a model whose computational cost only scales linearly with the number of atoms and which accurately describes all our experimental observations.

## II. EXPERIMENTAL SETUP

A schematic of the experimental setup is shown in Fig. 1(a). We optically interface cesium atoms with the evanescent field surrounding an optical nanofiber, which is realized as the waist of a tapered optical fiber with a nominal diameter of 500 nm. Using nanofiber-guided light,

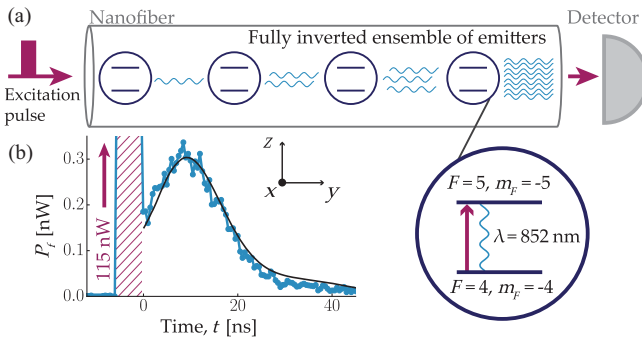


FIG. 1. (a) Schematic of the buildup of a superradiant burst in a cascaded system. Cesium atoms (blue circles) are trapped about 230 nm away from the nanofiber surface and are unidirectionally coupled to the evanescent field of the forward-propagating nanofiber-guided mode. This realizes a cascaded quantum system, where the dynamics of any atom can influence only downstream atoms. (b) We coherently invert an ensemble of about 1000 atoms using a forward-propagating nanofiber-guided optical pulse (purple arrow) and record the transmitted light. As the ensemble decays, we observe the emission of a superradiant burst into the forward-propagating mode. The solid black line represents the prediction of a cascaded interaction model; see main text.

we implement a two-color optical dipole trap that features two diametral arrays of trapping sites for the atoms, located about 230 nm away from the fiber surface. We probabilistically load atoms into this trapping potential from a magneto-optical trap [31]. Because of the collisional blockade effect, there will be at most one atom per trapping site [32,33]. We then apply a magnetic offset field of about 0.5 G in the  $z$  direction. Using a fiber-guided laser field that is near resonant with the  $|6S_{1/2}, F=4\rangle \rightarrow |6P_{3/2}, F=5\rangle$  D2 transition, we apply side-selective degenerate Raman cooling (DRC) to the atoms in one of the arrays [34], which are prepared in the outermost Zeeman state of the  $F=4$  hyperfine ground state manifold,  $|g\rangle = |6S_{1/2}, F=4, m_F=-4\rangle$ . This process simultaneously removes the atoms from the opposite trap array. After inferring the number of trapped atoms  $N$  via transmission spectroscopy [31], see Appendix A 1, we excite the atomic ensemble to the  $|e\rangle = |6P_{3/2}, F=5, m_F=-5\rangle$  state using a 4-ns-long fiber-guided optical pulse that is much shorter than the excited state lifetime of about 30 ns [35]. The excitation laser field is locally  $\sigma^-$  polarized [36,37] and resonant with the  $|g\rangle \rightarrow |e\rangle$  transition. We recently showed that this technique allows us to almost fully invert ensembles of up to 1000 atoms, with an excited state probability of about 80% [38]. Since the subsequently emitted light is  $\sigma^-$  polarized, the probability that a single atom emits into the locally almost perfectly  $\sigma^-$ -polarized forward-propagating mode is  $\beta_f \approx 0.01$ , about 10 times larger than the probability for backward emission [37]. We measure the power of the light that the atoms emit into the forward-propagating mode  $P_f$ ; see Appendix A 2. To obtain sufficient counting statistics, we excite the atoms 400 times per experimental sequence at a repetition rate of 5 kHz and average over several thousand sequences. During this probing, we switch from our fiber-guided DRC as described above to DRC with a free-space laser beam that is near resonant with the  $|6S_{1/2}, F=4\rangle \rightarrow |6P_{1/2}, F=4\rangle$  D1 transition. Since the corresponding scattering rate is much smaller than the collective decay rate of the atomic ensemble, we can continuously cool the atoms during the experimental sequence without disturbing their dynamics. Thanks to the continuous cooling, not more than 15% of the atoms are lost during the probing sequence with a duration of 80 ms.

## III. SUPERRADIANT BURST

In Fig. 1(b), we show an example time trace of  $P_f$  as blue dots. The 4 ns excitation pulse is switched off at time  $t=0$  ns. Subsequently, the ensemble of about 1000 inverted atoms decays, and we observe an initial increase of  $P_f$ . The power reaches a maximum value of  $P_f^{\max}$  after a delay of  $t_D \approx 9$  ns and then decreases. This initial increase in emitted power is in stark contrast to the exponential decay of independent atoms and is a characteristic feature

of a superradiant burst. We observe this burst notwithstanding the fact that the atoms are chirally coupled to the nanofiber. The synchronization of the atomic dipoles during their decay is enabled by the guided mode of the nanofiber, despite the large distance between atoms [39]. In addition, the unidirectional coupling makes the dynamics robust to the randomness of these distances. Since the size of the Hilbert space grows exponentially with the number of atoms, a numerical solution of the master equation describing the system, see Eq. (2) below, is prohibitively costly for as many as 1000 atoms. Instead, we developed a cascaded interaction model whose computational cost scales linearly with the number of atoms, and the result is shown as a black dashed line in Fig. 1(b). We describe this model, which agrees quantitatively with all data presented in this work, in detail below.

#### IV. SCALING WITH THE NUMBER OF ATOMS

The spontaneous synchronization of the atomic dipoles in our experiment is in competition with dephasing and decay into other modes [9]. As a result, the superradiant burst occurs only when the number of atoms exceeds a threshold, beyond which spontaneous synchronization dominates. To study this threshold, we measure the decay of fully inverted ensembles for varying atom numbers  $N$ ; see Figs. 2(a)–2(d). For  $N \sim 130$  in Fig. 2(a), we observe a monotonous decay of  $P_f$ , closely resembling the exponential decay expected for independently emitting atoms.

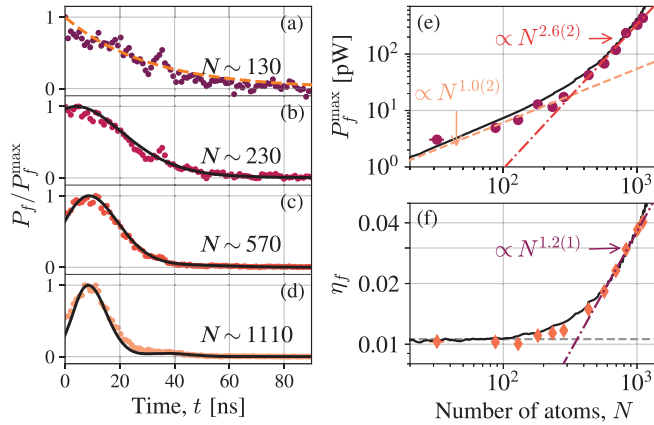


FIG. 2. (a)–(d) Power emitted by an inverted ensemble for different atom numbers  $N$ . As we increase  $N$ , the dynamics changes from an exponential decay to a superradiant burst. (e) Dependence of the peak-emitted power  $P_{\max}$  on  $N$  (purple dots). We observe a linear scaling for small  $N$  (orange dashed line), which becomes superlinear when  $N$  exceeds a threshold of about 300 (red dash-dotted line). (f) Dependence of the fraction of absorbed energy emitted into the forward-propagating mode  $\eta_f$  (orange diamonds) on  $N$ . Also here, we observe a threshold, below which  $\eta_f$  is constant and above which it increases with  $N$ . The corresponding model predictions are shown as solid black lines.

For  $N \sim 230$  in Fig. 2(b), we observe a plateau before  $P_f$  eventually decreases, indicating that the system is at the onset of a superradiant burst. For about 570 atoms, a clear burst is apparent, which is even more pronounced for about 1110 atoms. From these measurements, we extract the peak-emitted power  $P_f^{\max}$  and plot it as a function of the atom number  $N$  in Fig. 2(e). In this analysis, we first average  $P_f(t)$  over several thousand experimental runs and then determine the peak value of this averaged signal. Two regimes are clearly visible. For small  $N$ ,  $P_f^{\max}$  increases linearly, and a power-law fit reveals an exponent of 1.0(2). In this regime, the peak power occurs directly after switching off the excitation laser. Since all atoms emit independently, the power at the very beginning of the emission process is given by  $P_f^{\max} = P_f(t=0) = \Gamma_f E_{\text{st}}$ , where  $E_{\text{st}} \approx N\hbar\omega$  is the energy stored in the ensemble after the excitation pulse. This energy is radiated into the forward-propagating mode at a rate  $\Gamma_f = \beta_f \Gamma$ , where  $\Gamma/(2\pi) \approx 5.22$  MHz is the excited state decay rate. As  $N$  is increased further, the scaling changes, and the extracted exponent becomes 2.6(2). This threshold behavior and the superlinear scaling are indicative of a synchronization of the atomic dipoles, such that  $P_f^{\max}$  exceeds  $\Gamma_f E_{\text{st}}$ . Indeed, the change of the scaling of  $P_f^{\max}(N)$  is accompanied by the occurrence of burst dynamics; see Figs. 2(c) and 2(d). In the textbook case of the emission of a Dicke superradiant burst by a strongly confined ensemble, the scaling is quadratic since each atom constructively adds to the macroscopic dipole moment of the ensemble, and the power is proportional to its square [8]. There, the entire energy stored in the ensemble is emitted into a single spatial mode, regardless of whether the dipoles synchronize or not. However, in our experiment, a single atom emits only about 1% of its radiation into the (forward-propagating) guided mode, and about 99% of the light is scattered into the free-space modes. During the collective decay of the atoms, a phase pattern is formed across the atomic dipoles, which leads to constructive interference for emission into the forward-propagating mode. Therefore, the atoms emit into a narrower solid angle as  $N$  increases. Accordingly, a larger fraction of the radiated power is collected by the nanofiber-guided mode. This explains the faster-than-quadratic scaling beyond the threshold observed in our experiment. For further details on the scaling of  $P_f^{\max}$ , including in the limit of large  $N$ , see Appendix A 7.

In contrast to the weakly excited regime, where a similar phase pattern can be imprinted on the ensemble by an external laser field [40–43], here, this pattern forms spontaneously, as we show further below. We further analyze the collective enhancement of forward scattering by measuring the fraction of the stored energy that is emitted into the forward-propagating mode  $\eta_f$  [38]. We plot  $\eta_f$  as a function of  $N$  in Fig. 2(f) and find a similar threshold behavior as for the peak power  $P_f^{\max}$ . For small  $N$ ,  $\eta_f$  stays

at a constant value of about  $0.01 \approx \beta_f$ , as expected for independently emitting atoms; see dashed gray line in Fig. 2(f). For larger atom numbers,  $\eta_f$  increases as  $N^{1.2(1)}$ ; i.e., forward scattering is indeed collectively enhanced compared to independent decay. We note that we expect  $\eta_f$  to saturate for even larger  $N$ ; see Appendix A 7.

## V. DEPENDENCE ON THE INITIAL STATE

We now explore the dynamics of the superradiant burst for different initial states of the atomic ensemble consisting of about 1000 atoms. By exciting an atom  $k$  with a short, resonant optical pulse of pulse area  $A_k$ , we prepare it to good approximation in a coherent superposition of ground and excited state [38],

$$|\psi_k\rangle = \cos\left(\frac{A_k}{2}\right)|g\rangle - i \sin\left(\frac{A_k}{2}\right)|e\rangle, \quad (1)$$

where we have chosen a frame that rotates with the forward-propagating laser mode. The time traces of the emitted power  $P_f$  are shown as a function of  $\bar{A}$  in Fig. 3(a), where each time trace is normalized to its peak value  $P_f^{\max}$ . Here,  $\bar{A}$  is the mean pulse area “seen” by the first atom that interacts with the excitation pulse and takes into account the averaging over the distribution of coupling strengths between the atom and the waveguide mode; see the Appendixes A 5 and A 6. We extract the time at which the maximal power is emitted into the nanofiber  $t_D$  and display it as the black dashed line. For small pulse areas ( $\bar{A} < 0.7\pi$ ), the power decreases monotonously as the ensemble decays, and  $t_D = 0$ . However, for  $\bar{A}$  between about  $0.7\pi$  and  $1.3\pi$ , the ensemble is substantially inverted and a superradiant burst is apparent, such that  $t_D > 0$ . The closer the ensemble is to full inversion, the longer the delay  $t_D$ , with a maximal value of  $t_D \approx 9$  ns. When  $\bar{A}$  is further increased beyond  $1.3\pi$ , the ensemble is coherently

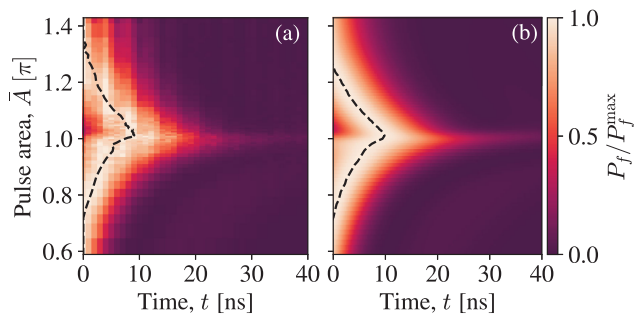


FIG. 3. Dynamics of the power emitted into the nanofiber-guided mode  $P_f$  for different pulse areas seen by the first atom  $\bar{A}$ . Each time trace is normalized to its peak value  $P_f^{\max}$ . The time at which the maximum is reached  $t_D$  is indicated by the black dashed lines. Panel (a) shows the measured data, while panel (b) shows the corresponding model predictions.

deexcited and the burst gradually vanishes. As one would expect, we observe maximal inversion and thus the largest delay for  $\bar{A} \approx \pi$ . Details on how experimental imperfections influence the burst dynamics can be found in Appendix A 6. In Fig. 3(b), we show the corresponding model prediction and find quantitative agreement, confirming that our cascaded interaction model captures the essential physical mechanism, which determines the system dynamics.

## VI. FIRST-ORDER COHERENCE PROPERTIES

To understand the role of coherence of the superradiant burst in our system, we measure the complex-valued normalized first-order coherence function of the forward-propagating light  $g^{(1)}(t_1, \tau)$ . Since we analyze a nonstationary field,  $g^{(1)}(t_1, \tau)$  depends explicitly on two times,  $t_1$  and  $t_1 + \tau$  [44] (the excitation pulse is switched off at  $t = t_1 = 0$  ns, cf. Fig. 1). We superpose the light emitted into the forward-propagating mode with a local oscillator (LO) that is derived from the excitation laser and detuned by  $\omega_{\text{LO}} = 2\pi \times 230$  MHz. The intensity-intensity correlations of the resulting heterodyne signal contain a beating pattern, whose visibility is a measure of  $g^{(1)}(t_1, \tau)$ . Specifically, the normalized beating pattern is given by  $\text{Re}\{e^{-i\omega_{\text{LO}}\tau} g^{(1)}(t_1, \tau)\}$ , where  $\text{Re}\{\cdot\}$  denotes the real part; see Appendix A 3. In Figs. 4(a)–4(c), we plot the measured beating patterns for three different pulse areas  $\bar{A}$  and for two different times  $t_1$ . Throughout the considered parameter space, we observe that the beating pattern is well described by a function of the form  $\mathcal{X}(t_1) \cos(\omega_{\text{LO}}\tau)$ ; i.e.,  $g^{(1)}(t_1, \tau)$  is real valued. The amplitude  $\mathcal{X}(t_1)$  thus quantifies the time-averaged first-order coherence. While full first-order coherence would in principle lead to  $|\mathcal{X}(t_1)| = 1$ , a polarization mismatch between the LO and the signal field reduces the visibility in our experiment, so that a fully coherent signal field leads only to  $|\mathcal{X}(t_1)| \approx 0.5$ ; see Appendix A 3 for details.

In the top of panels Figs. 4(a)–4(c), we set  $t_1 = -2$  ns (i.e., when the excitation pulse is still on) and  $\tau > 2$  ns (i.e., during the superradiant burst). Consequently, the interference signal corresponds to a cross-correlation between the excitation laser light and the superradiant burst emitted by the atoms. In Fig. 4(a),  $\bar{A} < \pi$ , and we observe a beating pattern with near maximum visibility,  $\mathcal{X}(t_1) \approx -0.5$ , indicating that the emitted light is coherent with respect to the excitation laser field. Here,  $\mathcal{X}(t_1)$  is negative, because the burst light emitted by the atoms is phase shifted by  $\pi$  with respect to the laser, as expected. In Fig. 4(c), the ensemble is coherently driven beyond full inversion ( $\bar{A} > \pi$ ), and the atoms radiate in phase with the laser, indicated by  $\mathcal{X}(t_1) \approx +0.5$ . Importantly, however, for maximal inversion as shown in Fig. 4(b), we do not observe any interference fringes,  $\mathcal{X}(t_1) \approx 0.0$ ; i.e., the emitted light features no fixed phase relationship with respect to the excitation laser field. In Fig. 4(d), we plot  $|\mathcal{X}(t_1 = -2 \text{ ns})|$

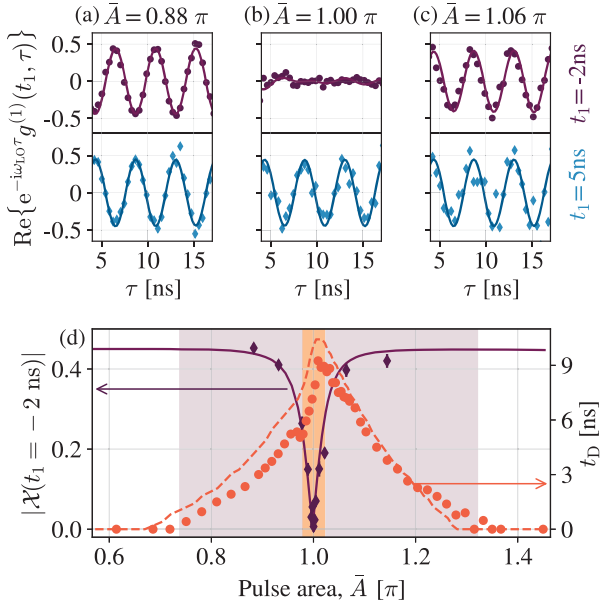


FIG. 4. Heterodyne analysis of the first-order coherence  $g^{(1)}(t_1, \tau)$  of the forward-emitted light, modulated with the local oscillator detuning of  $\omega_{LO} = 2\pi \times 230$  MHz as a function of the pulse area  $\bar{A}$ . The model predictions are shown as solid lines. In the top of panels (a)–(c),  $t_1 = -2$  ns lies within the excitation pulse. The  $g^{(1)}$  function is thus given by the cross-correlation of the excitation laser and the burst light. In (b), when maximal inversion is reached, the oscillations disappear, indicating that there is no fixed phase relationship between fluorescence and excitation laser. In the bottom panels of (a)–(c),  $t_1 = 5$  ns lies within the burst. The interference fringes indicate that the superradiant emission is first-order coherent for all considered values of  $\bar{A}$ . (d) Magnitude of the coherence of the emitted light with respect to the laser  $|\mathcal{X}|$  for different  $\bar{A}$  (purple diamonds on left-hand axis), and time delay of the maximum of the superradiant burst  $t_D$  (orange dots on right-hand axis).

as a function of the pulse area  $\bar{A}$  (purple diamonds). In addition, we show the delay time  $t_D$  at which the peak power  $P_f^{\max}$  is emitted (orange dots). These are the same data shown as a black dashed line in Fig. 3(a). We observe that the minimum of  $|\mathcal{X}|$  appears when  $t_D$  reaches its largest value, i.e., when the ensemble is maximally inverted. Interestingly, the coherence with respect to the laser features a dip which is much narrower than the region in which  $t_D$  is larger than zero. This allows us to identify two regimes of superradiant burst dynamics in our experiment. In the first regime close to full inversion, indicated by the light red shaded area, the superradiant burst is incoherent with respect to the excitation laser and is therefore triggered by vacuum fluctuations. In this case, one also speaks of superfluorescence [45]. In a second regime comprising a much broader range of pulse areas indicated by the light purple shaded regions, the burst is coherent with the excitation laser. Here, the phase is imprinted onto the ensemble by the excitation laser field.

In the lower row of Figs. 4(a)–4(c), we set  $t_1 = 5$  ns (i.e., after the excitation pulse has been switched off), thereby measuring the first-order coherence of the superradiant burst. We observe that  $\mathcal{X}(t_1) \approx 0.5$  including for  $\bar{A} = \pi$  in Fig. 4(b). There, the atomic ensemble is maximally inverted, has effectively no total dipole moment, and is thus incoherent with respect to any external reference; see Appendix A 6. This indicates that even the vacuum-induced superradiant burst is predominantly emitted into a single temporal mode [46]. Such a behavior has recently been predicted for Dicke superradiance of ensembles of two-level systems that are coupled symmetrically [23,47], but has, to our knowledge, not been confirmed experimentally so far.

Let us now discuss the observation of an interference pattern in the heterodyne measurement of the vacuum-induced burst in the context of the theory of heterodyne detection of a quantum mechanical, single field mode  $\hat{E}$ . In a Heisenberg picture, where quantum operators depend on time, the autocorrelation function of the heterodyne photocurrent is a measure for the correlator,  $G^{(1)}(t_1, \tau) = \langle \hat{E}^\dagger(t_1 + \tau) \hat{E}(t_1) \rangle$  [48], as defined by Glauber [49]. In an equivalent Schrödinger picture, where operators are time independent, however, this interference is a consequence of a nonvanishing dipole moment appearing in the conditional atomic quantum state during the heterodyne measurement [50–52]. While a quantitative modeling of our experiment along these lines is beyond the scope of the present work, we do present a theoretical study of a fully inverted ensemble of independently emitting atoms in Appendix A 4. Interestingly, also in this situation, the emitted field is predicted to feature full coherence, similar to our observations.

## VII. THEORETICAL MODEL

Let us now turn to the theoretical description of our system. The many-body master equation for the density operator  $\hat{\rho}$  of  $N$  atoms, which are coupled to a unidirectional waveguide, is given by [26,27,29,53,54]

$$\frac{d}{dt} \hat{\rho} = -\frac{i}{\hbar} [\hat{H}_{\text{casc}}, \hat{\rho}] + \Gamma_f \mathcal{L}_{\text{coll}}[\hat{\rho}] + \Gamma_0 \mathcal{L}_0[\hat{\rho}], \quad (2)$$

with the cascaded interaction Hamiltonian,

$$\hat{H}_{\text{casc}} = -i \frac{\hbar \Gamma_f}{2} \sum_{k < l} \hat{\sigma}_l^\dagger \hat{\sigma}_k + \text{H.c.} \quad (3)$$

Here,  $\hat{\sigma}_k = |g\rangle_k \langle e|_k$  is the spin lowering operator of the  $k$ th atom in a frame which corotates with the forward-propagating mode with  $k = 1, \dots, N$ . The indices are increasing in the direction of the propagating mode. Importantly, this Hamiltonian allows information to propagate in only one direction along the waveguide.

The collective decay into the waveguide with rate  $\Gamma_f = \beta_f \Gamma$  is described by Lindblad superoperator  $\mathcal{L}_{\text{coll}}[\hat{\rho}]$ , while independent decay into free space with rate  $\Gamma_0 = (1 - \beta)\Gamma$  is described by  $\mathcal{L}_0[\hat{\rho}]$ ,

$$\mathcal{L}_{\text{coll}}[\hat{\rho}] = \frac{1}{2} \sum_{k,l} (2\hat{\sigma}_l \hat{\rho} \hat{\sigma}_k^\dagger - \hat{\sigma}_k^\dagger \hat{\sigma}_l \hat{\rho} - \hat{\rho} \hat{\sigma}_k^\dagger \hat{\sigma}_l), \quad (4a)$$

$$\mathcal{L}_0[\hat{\rho}] = \frac{1}{2} \sum_k (2\hat{\sigma}_k \hat{\rho} \hat{\sigma}_k^\dagger - \hat{\sigma}_k^\dagger \hat{\sigma}_k \hat{\rho} - \hat{\rho} \hat{\sigma}_k^\dagger \hat{\sigma}_k). \quad (4b)$$

We note that while the many-body master equation, Eq. (2), is useful for understanding the physical properties of the system, its solution is inaccessible for as many as  $N = 1000$  coupled atoms, since the size of the density matrix  $\hat{\rho}$  scales exponentially with  $N$ . In order to approximate the solution numerically, let us note that the dynamics of each individual atom in the ensemble is described by the quantum Langevin equation [55],

$$\frac{d}{dt} \hat{\sigma}_k = -\frac{\Gamma}{2} \hat{\sigma}_k - i\sqrt{\Gamma_f}(1 - 2\hat{\sigma}_k^\dagger \hat{\sigma}_k) \hat{a}_k(t), \quad (5)$$

where  $\hat{a}_k(t)$  is the annihilation operator of the waveguided light field before the  $k$ th atom. Because of the cascaded interaction, the output field of this mode serves as the next atom's input,  $\hat{a}_{k+1}(t)$ , and is given by the input-output equation [55]:

$$\hat{a}_{k+1}(t) = \hat{a}_k(t) - i\sqrt{\Gamma_f} \hat{\sigma}_k. \quad (6)$$

For our cascaded quantum system, these equations are equivalent to the master equation (2) [6,7]. In Ref. [38], we approximated the photonic states between the atoms as coherent states; i.e., we replaced  $\hat{a}_k(t)$  by its amplitude  $\alpha_k(t) = \langle \hat{a}_k(t) \rangle$ . This reduces the Langevin equation of the  $k$ th atom to the (single-atom) optical Bloch equations and allows one to solve the mean-field atomic dynamics of the whole ensemble with linear computational complexity. However, it is well known that the output field  $\hat{a}_{k+1}$  is in general no longer in a coherent state. In particular, close to full inversion there is no coherence left for zero input field. Therefore, the total output flux,  $P_{k+1}(t) = \langle \hat{a}_{k+1}^\dagger \hat{a}_{k+1} \rangle(t)$ , is always larger than the coherent part,  $P_{k+1}^c(t) = |\langle \hat{a}_{k+1} \rangle(t)|^2$ . The difference  $P_{k+1}^{\text{inc}}(t) = P_{k+1}(t) - P_{k+1}^c(t)$  is commonly referred to as the ‘‘incoherent’’ part of the emitted light, which is due to spontaneous emission. In order to describe this incoherent driving of the next atom, we model the input field  $\hat{a}_k(t)$  as the superposition of a coherent field and a ‘‘randomly phased laser field’’ [56]. The density operator of such a field is given by

$$\hat{\rho}_L(t) = \frac{1}{2\pi} \int_0^{2\pi} d\phi |\alpha(\phi, t)\rangle \langle \alpha(\phi, t)|, \quad (7)$$

which represents a mixture of coherent states with amplitudes  $\alpha(\phi, t) = \sqrt{P_k^c(t)} + e^{i\phi} \sqrt{P_k^{\text{inc}}(t)}$ , homogeneously sampled over the phase  $\phi$ . This ‘‘mixed coherent state’’ has the property that its total power  $\langle \hat{a}_k^\dagger \hat{a}_k \rangle(t) = P_k^c(t) + P_k^{\text{inc}}(t)$  is larger than its coherent part  $|\langle \hat{a}_k \rangle(t)|^2 = P_k^c(t)$ . Moreover, we can still straightforwardly solve the atomic dynamics of the  $k$ th atom given this input state by solving the optical Bloch equation for each phase  $\phi$  separately. We then numerically compute the output's coherent and incoherent parts,  $P_{k+1}^c(t)$  and  $P_{k+1}^{\text{inc}}(t)$ , respectively, by averaging over  $\phi$ . We apply this method iteratively to each atom and finally obtain the output power  $P_f(t) = P_{N+1}(t)$ . The computational complexity of this method is thus linear in  $N$ .

In addition, we average the simulated time traces over a truncated Gaussian distribution of  $\beta_f$  values to account for the thermal distribution of atoms in the trapping potential and, thus, the varying distances of the atoms to the nanofiber surface. We fit the corresponding mean and standard deviation of the probability distribution  $p(\beta_f)$  to the experimental data, yielding  $\langle \beta_f \rangle = 0.011$  and  $\sigma_\beta = 0.0067$ , respectively [38]; see Appendix A 5. Notably, we only need these two free parameters to obtain quantitative agreement with the data throughout the whole parameter space studied in this work. We numerically confirmed that the finite duration of the excitation pulse and the inhomogeneous spread of coupling strengths does not qualitatively alter the observed dynamics; see Appendix A 6 for further detail. The quantitative agreement of our model with the data attests that our system can indeed be modeled as a cascaded quantum system and that our mixed coherent state approximation is justified. Other methods that account for incoherent dynamics beyond the mean field typically rely on higher-order cumulant expansions [57]. To our knowledge, while these models are solvable in polynomial time, the solution for more than a few hundred atoms remains elusive.

## VIII. CONCLUSIONS AND OUTLOOK

In conclusion, we have experimentally observed the emission of superradiant bursts by an ensemble of atoms that is unidirectionally coupled to a guided mode of an optical nanofiber. Our results demonstrate that superradiance prevails in a cascaded quantum system, despite the reduced symmetry of the light-matter coupling. The scaling of the peak power of the burst with the number of atoms is observed to be faster than in the Dicke case, which we could explain in an intuitive way. Lastly, we presented a direct measurement of the coherence of the burst and its dependence on the initially prepared atomic state, experimentally demonstrating a textbook prediction. Notably, this allowed us to show that the superradiant burst is predominantly emitted into a single temporal mode, thereby demonstrating an important prerequisite for

generating multiphoton Fock states with high fidelity, which may, e.g., turn out useful in quantum metrology [47,58]. In addition, it has been proposed that even more complex, entangled states can be generated by mapping an atomic state to a photonic state using the collective response of waveguide-coupled atoms [59,60]. Finally, all data shown in this work are in quantitative agreement with a model prediction, which is made possible by the fact that we deal with a cascaded quantum system, resulting in a drastic reduction of the computational complexity compared to the exponential scaling of the many-body master equation.

Future research directions include the experimental investigation of the second-order coherence of the burst [61]. It would also be interesting to study the long-term dynamics of the decay. Here, subradiant features related to a high degree of correlations between the atomic dipoles are expected. For continuous driving, a superradiant phase transition has recently been observed with an atomic ensemble emitting into free space [62]. When chirally coupled atoms are driven continuously, steady-state many-body entanglement between the emitters is predicted to occur [26,63]. The search for and experimental investigation of robust entanglement signatures in systems like ours therefore constitute another promising research avenue. Finally, placing the atoms in a nanofiber-integrated optical resonator would yield a versatile test bed for studying the physical mechanism underlying a superradiant laser [13,64].

## ACKNOWLEDGMENTS

We thank A. Asenjo García, A. Browaeys, S. Cardenas López, J. I. Cirac, I. Ferrier-Barbut, K. Hammerer, K. Kusmierk, S. Masson, K. Mølmer, L. A. Orozco, J. Volz, and L. P. Yatsenko for stimulating discussions and helpful comments. We acknowledge funding by the Alexander von Humboldt Foundation in the framework of the Alexander von Humboldt Professorship endowed by the Federal Ministry of Education and Research, as well as funding by the European Commission under the project DAALI (Grant No. 899275).

## APPENDIX

### 1. Loading of the nanofiber-based atom trap

We load cesium atoms into a magneto-optical trap (MOT) and perform optical molasses cooling to transfer the atoms into the nanofiber-based trapping potential, which features two diametral arrays of trapping sites [31]. The trapping potential is created by a running-wave blue-detuned nanofiber-guided field (wavelength 760 nm, power 20.5 mW) and a standing-wave red-detuned field (wavelength 1064 nm, total power 2.4 mW). The loading is probabilistic and, due to the collisional blockade effect, each potential minimum is occupied by at most one

atom [32]. Then we apply a homogeneous magnetic offset field of about 0.5 G along  $+z$  (see Fig. 1 in the main text) and further cool the atoms on one side of the nanofiber by degenerate Raman cooling using nanofiber-guided light that is near resonant with the  $|6S_{1/2}, F=4\rangle \rightarrow |6P_{3/2}, F=5\rangle$  D2 transition [34]. At the same time, the atoms on the other side of the nanofiber are subject to degenerate Raman heating and are expelled from the trap, such that we are left with a one-dimensional array of atoms on only one side of the nanofiber. After these preparation steps, we switch off both the MOT and DRC laser fields such that during the subsequent measurements there is no resonant light present at a wavelength of 852 nm, except for the excitation laser. As described in the main text, we then use an additional free-space laser resonant with the D1 transition at a wavelength of 894 nm in order to continuously cool the trapped atoms by DRC. The number of trapped atoms  $N$  can be tuned by changing the MOT loading time, which ranges from 80 ms to 7 s in our experiment.

### 2. Detection setup

Figure 5 schematically depicts the detection setup that we use to measure the power of the light exiting the waveguide in the forward direction. We first spectrally filter the signal field at a wavelength of 852 nm by suppressing the trapping light fields and other background light using a volume Bragg grating. The light is first split by a 50:50 beam splitter and then further separated by a 10:90 ( $R:T$ ) beam splitter. To further suppress the background, each beam then passes a bandpass filter that is centered around 852 nm. We detect the light at the different output ports of the beam splitters using two fiber-coupled single photon

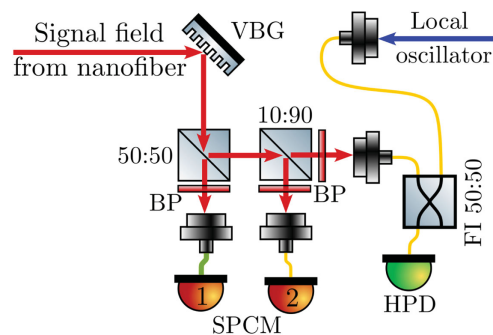


FIG. 5. Schematic of the detection setup. The signal field is spectrally filtered around a wavelength of 852 nm using a volume Bragg grating (VBG) and a bandpass filter (BP) in front of each fiber-coupled detector. The yellow and green lines depict single-mode and multimode fibers, respectively. We measure the power of the signal field using two single photon counting modules (SPCM) and a hybrid photodetector (HPD). The light incident on the HPD can be overlapped with a local oscillator using a fiber-integrated 50:50 beam splitter (FI 50:50). The frequency of the local oscillator field is shifted by 230 MHz with respect to the excitation laser field.

counting modules (SPCM 1 and SPCM 2) and a fiber-coupled hybrid photodetector (HPD). We use SPCM 1 to measure the probe transmission spectrum, from which we infer the optical depth of the atomic ensemble and the number of trapped atoms. For the experiments shown in this paper, we expose the atomic ensemble to intense optical pulses, which have a power that is several orders of magnitude larger than the power emitted by the ensemble during its decay. Since our SPCMs have a dead time of about 25 ns, we have to substantially attenuate the power incident on the SPCMs in order to detect the fluorescence that follows the intense excitation pulse. In contrast, the HPD features a much shorter dead time of only about 2 ns. We can therefore saturate the HPD during the excitation pulse and still detect the fluorescence signal. The signal of the HPD is strongly saturated during the excitation pulse. Therefore, we use the signal from SPCM 2 to extract the fraction of absorbed energy that is emitted into the forward direction by the atoms  $\eta_f$ . To ensure that the excitation pulse does not saturate the signal from SPCM 2, we attenuate the light incident on SPCM 2 using neutral density filters (not shown).

For the measurements presented in Sec. VI, we superimpose the signal incident on the HPD with a local oscillator light field using a fiber-integrated 50:50 beam splitter. We derive the local oscillator field from the excitation laser field and shift its frequency by 230 MHz. While performing the heterodyne measurements, we also record the bare signal field (without local oscillator) using SPCM 2. We use the resulting time traces to normalize the first-order coherence function that we extract from the heterodyne signal; see below.

### 3. Extraction of the first-order coherence function from the heterodyne signal

The first- and second-order correlation functions of a light field  $\hat{a}(t)$  with power  $P(t) = \langle \hat{a}^\dagger(t)\hat{a}(t) \rangle$  are defined as [44]

$$\begin{aligned} G^{(1)}(t, \tau) &= \langle \hat{a}^\dagger(t)\hat{a}(t+\tau) \rangle, \\ g^{(1)}(t, \tau) &= \frac{G^{(1)}(t, \tau)}{\sqrt{P(t)P(t+\tau)}}, \\ G^{(2)}(t, \tau) &= \langle \hat{a}^\dagger(t)\hat{a}^\dagger(t+\tau)\hat{a}(t+\tau)\hat{a}(t) \rangle, \\ g^{(2)}(t, \tau) &= \frac{G^{(2)}(t, \tau)}{P(t)P(t+\tau)}. \end{aligned} \quad (\text{A1})$$

Here,  $g^{(1)}$  and  $g^{(2)}$  denote the normalized first-order and second-order correlation functions, respectively. Note that for a nonstationary case, such as the one we analyze, these correlators explicitly depend on two time instances,  $t$  and  $t + \tau$ . Let us assume a light field  $\hat{a}(t)$  with power  $P(t)$  that describes the nanofiber-guided mode and superpose a classical, continuous-wave local oscillator field  $a_{\text{LO}}$  with

power  $P_{\text{LO}}$ , with a random relative phase  $\theta_{\text{LO}}$  and relative frequency  $\omega_{\text{LO}}$ :

$$a_{\text{LO}}(t) = \sqrt{P_{\text{LO}}}e^{i(\omega_{\text{LO}}t + \theta_{\text{LO}})}. \quad (\text{A2})$$

The field incident on the detector and its power are then given by

$$\hat{a}_D(t) = \sqrt{P_{\text{LO}}}e^{i(\omega_{\text{LO}}t + \theta_{\text{LO}})} + \hat{a}(t), \quad (\text{A3})$$

$$P_D(t) = P_{\text{LO}} + P(t). \quad (\text{A4})$$

In our experiment, we measure the normalized second-order correlation function of this heterodyne signal. We average over the relative phase between the local oscillator and the signal field  $\theta_{\text{LO}}$ , since the latter is not stabilized and drifts randomly on the timescale of the repetition period of our measurements. Because of these random drifts, there is no interference term in Eq. (A4) since it averages to zero. Using the definitions in Eq. (A1), we obtain the normalized second-order autocorrelation function of the heterodyne signal:

$$\begin{aligned} g_D^{(2)}(t, \tau) &= 1 + \frac{2P_{\text{LO}}\sqrt{P(t)P(t+\tau)}}{P_D(t)P_D(t+\tau)}\text{Re}\{e^{-i\omega_{\text{LO}}\tau}g^{(1)}(t, \tau)\} \\ &\quad + \frac{P(t)P(t+\tau)}{P_D(t)P_D(t+\tau)}[g^{(2)}(t, \tau) - 1]. \end{aligned} \quad (\text{A5})$$

Since, for the experimental parameters in our experiment,  $P_{\text{LO}} \gg \sqrt{P(t)P(t+\tau)}$ , we neglect the last term that includes the contribution of  $g^{(2)}(t, \tau)$  such that we are left with

$$g_D^{(2)}(t, \tau) = 1 + V_{\text{max}}(t, \tau)\text{Re}\{e^{-i\omega_{\text{LO}}\tau}g^{(1)}(t, \tau)\}. \quad (\text{A6})$$

Here, we have introduced the maximum visibility:

$$V_{\text{max}}(t, \tau) = \frac{2P_{\text{LO}}\sqrt{P(t)P(t+\tau)}}{P_D(t)P_D(t+\tau)}. \quad (\text{A7})$$

The second-order correlation function of our heterodyne signal is thus given by the first-order correlation function of the signal field  $\hat{a}(t)$ , oscillating at  $\omega_{\text{LO}}$ . We extract  $g_D^{(2)}(t, \tau)$  and then  $V_{\text{max}}(t, \tau)$  from our measurements and infer the following quantity from our data:

$$\text{Re}\{e^{-i\omega_{\text{LO}}\tau}g^{(1)}(t, \tau)\} = \frac{g_D^{(2)}(t, \tau) - 1}{V_{\text{max}}(t, \tau)}, \quad (\text{A8})$$

which we show in Fig. 4 of the main text. Note that in this work we drive the atomic ensemble on resonance such that

$g^{(1)}$  is real valued. As discussed in the main text, it can be both negative (for excitation pulse areas below  $\pi$ ) and positive (for excitation pulse areas above  $\pi$ ). Because of an imperfect overlap between the polarizations of the signal field and the local oscillator field, the maximal visibility in the experiment is further reduced. We experimentally checked that the oscillations shown in Fig. 4 of the main text indeed reach maximal contrast if a polarization filter is placed in front of the detector.

#### 4. First-order coherence of independently decaying atoms

Consider a single two-level system with lowering operator  $\hat{\sigma} = |g\rangle\langle e|$ , which is excited at time  $t = 0$ , and which decays through spontaneous emission with rate  $\gamma$ . Using standard techniques, we find the following time-dependent correlators [65]:

$$\langle \hat{\sigma}(t) \rangle = 0, \quad (\text{A9a})$$

$$\langle \hat{\sigma}^\dagger(t) \hat{\sigma}(t) \rangle = e^{-\gamma t}, \quad (\text{A9b})$$

$$\langle \hat{\sigma}^\dagger(t) \hat{\sigma}(t + \tau) \rangle = e^{-\gamma t - \gamma \tau / 2}. \quad (\text{A9c})$$

Here, we consider a rotating frame at the transition frequency of the atom. If we now consider the emitted field  $\hat{a} = r \hat{\sigma}$  with some coupling constant  $r$ , we find the normalized, first-order correlation function of  $\hat{a}(t)$  as

$$g^{(1)}(t, \tau) = \frac{\langle \hat{\sigma}^\dagger(t) \hat{\sigma}(t + \tau) \rangle}{\sqrt{\langle \hat{\sigma}^\dagger \hat{\sigma} \rangle(t) \langle \hat{\sigma}^\dagger \hat{\sigma} \rangle(t + \tau)}} = 1. \quad (\text{A10})$$

The field emitted by a single, excited atom is thus first-order coherent; i.e., it is emitted into a single temporal mode [46].

Next, we consider  $N$  atoms which are all prepared in the excited state. Let us assume that the scattered light of the atoms couples to a single optical mode  $\hat{a}$ , which is given by

$$\hat{a}(t) = \sum_{n=1}^N r_n \hat{\sigma}_n(t). \quad (\text{A11})$$

Here,  $r_n$  are the individual coupling constants of the atoms to that mode, and  $\hat{\sigma}_n$  is the lowering operator of the  $n$ th atom. We assume independent dynamics of the atoms; that is, the emitted field of any atom cannot influence the dynamics of any other atom. Because of the independence, we have for  $m \neq n$ :  $\langle \hat{\sigma}_m^\dagger(t) \hat{\sigma}_n(t + \tau) \rangle = \langle \hat{\sigma}_m^\dagger(t) \rangle \langle \hat{\sigma}_n(t + \tau) \rangle = 0$ . With this, we find the first-order coherence function of  $\hat{a}(t)$  as

$$\langle \hat{a}^\dagger(t) \hat{a}(t + \tau) \rangle = \sum_{n=1}^N |r_n|^2 \langle \hat{\sigma}_n^\dagger(t) \hat{\sigma}_n(t + \tau) \rangle. \quad (\text{A12})$$

Since all atoms are excited at the same time, the correlators  $\langle \hat{\sigma}_n^\dagger(t) \hat{\sigma}_n(t + \tau) \rangle$  are identical to Eq. (A9c) and independent of  $n$ . From this, it follows directly that also in the case of many independent atoms,  $g^{(1)}(t, \tau) = 1$ .

#### 5. Inhomogeneous broadening of the coupling strength $\beta_f$

Since the atoms couple to the evanescent field of the nanofiber-guided mode, the coupling strength of each individual atom depends on its radial distance from the nanofiber surface. Because of the thermal motion of the atoms in the traps, this radial distance and, consequently, the atom-waveguide coupling strength  $\beta_f$  vary. Moreover, the scattering of photons from the 400 excitation pulses sent per experimental sequence leads to a small temperature increase of the atoms during the measurements. While the coupling strength of each trapped atom changes between consecutive excitation pulses, we expect it to be approximately constant during one cycle of excitation and collective decay. This is due to the latter dynamics being about a thousand times faster than the center-of-mass motion of atoms in the nanofiber-based trap. In order to model the inhomogeneous coupling strength in our numerical simulation, we assume a Gaussian probability distribution of  $\beta_f$  values  $p(\beta_f)$ . We ensure that  $\beta_f$  takes only physically meaningful values by truncating the distribution below  $\beta_f = 0$  and above  $\beta_f = 1$ . The distribution is shown in Fig. 6.

In order to model the experimental results, we draw a random value of  $\beta_f$  for each atom from this probability distribution and then compute the propagation of the light field through the ensemble of atoms using our cascaded interaction model. We repeat this process 100 times and average the resulting model predictions. We then fit the predictions to the experimental data shown in Fig. 3 of the main text by varying the mean of the truncated distribution

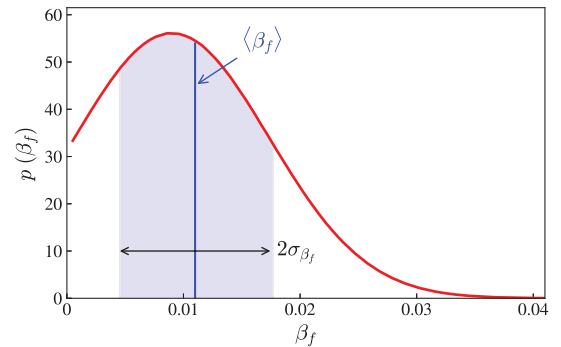


FIG. 6. Probability distribution used to model the temperature-induced variation of the atom-waveguide coupling strength  $\beta_f$ . The mean value,  $\langle \beta_f \rangle = 0.011$ , and the standard deviation,  $\sigma_{\beta_f} = 0.0067$ , of the truncated Gaussian distribution obtained from fitting the experimental data are shown as the blue vertical line and the black double arrow, respectively.

$\langle\beta_f\rangle$  and its standard deviation  $\sigma_{\beta_f}$ , yielding optimal parameters  $\langle\beta_f\rangle = 0.011$  and  $\sigma_{\beta_f} = 0.0067$ , respectively. These values are almost identical to those reported in Ref. [38].

## 6. Imperfect state preparation

Ideally, we want to initialize each atom in the same coherent superposition of ground and excited state:

$$|\psi\rangle_{\text{ideal}} = \cos\left(\frac{A}{2}\right)|g\rangle - i\sin\left(\frac{A}{2}\right)|e\rangle. \quad (\text{A13})$$

The pulse area  $A$  is the product of the Rabi frequency  $\Omega$  and the pulse duration  $T_{\text{pulse}}$ , i.e.,  $A = \Omega T_{\text{pulse}}$ . For an atom coupled with strength  $\beta_f$  to the nanofiber-guided mode, we find

$$A = \sqrt{\frac{4\beta_f\Gamma P_{\text{pulse}}}{\hbar\omega}} T_{\text{pulse}} \quad (\text{A14})$$

$$= C\sqrt{\beta_f}, \quad (\text{A15})$$

where  $P_{\text{pulse}}$  is the power of the excitation pulse,  $\hbar\omega$  is the photon energy, and  $C$  is a shorthand notation used in the following. Two effects reduce the fidelity of preparing the state of Eq. (A13) for pulsed excitation. First, spontaneous decay during the excitation is only negligible for pulse durations  $T_{\text{pulse}} \ll 1/\Gamma$ . Second, for a distribution  $p(\beta_f)$  of coupling strengths to the optical mode, the pulse duration and optical power can only be optimized for one specific value of  $\beta_f$ , resulting in imperfect state preparation if the atom has another coupling strength.

When dealing with many atoms, the decrease of the pulse power along the nanofiber-trapped atomic ensemble needs to be considered in addition, since each atom absorbs light from the excitation pulse. In this section, we study how these effects influence our experimental results. Note that the effect of absorption could be eliminated by exciting the ensemble with a suitably chosen free-space laser beam [66].

### a. Average excitation of one atom

Regarding the effects arising from the inhomogeneous distribution of coupling strengths  $\beta_f$  in our experiment, we first consider one atom, which is excited by consecutive laser pulses, each time with a different value of  $\beta_f$  drawn from the distribution  $p(\beta_f)$ . We consider the mean pulse area  $\bar{A}$ , which serves as a characteristic parameter in several of our measurements. We also discuss how quantities such as the mean excitation probability depend on the experimental parameters. In order to keep the notation concise throughout the paper, we omit to explicitly indicate the averaging for quantities such as the atomic excitation probability or the dipole moment.

We can calculate the mean pulse area  $\bar{A}$  by averaging Eq. (A15) over the distribution  $p(\beta_f)$ :

$$\bar{A} = C \int_0^1 \sqrt{\beta_f} p(\beta_f) d\beta_f. \quad (\text{A16})$$

For a given value of  $\beta_f$ , the pulse area  $A(\beta_f)$  can now be expressed as

$$A(\beta_f) = \bar{A} \frac{\sqrt{\beta_f}}{\langle\sqrt{\beta_f}\rangle}, \quad (\text{A17})$$

where  $\langle\sqrt{\beta_f}\rangle$  is the mean value of  $\sqrt{\beta_f}$ . Equation (A17) enters in our theory predictions for the burst dynamics in the presence of inhomogeneous broadening, and  $\bar{A}$  is used as characteristic parameter, e.g., in Figs. 3 and 4.

In Fig. 7(a), we show the mean excited state probability  $p_{\text{exc}}$  as a function of  $\bar{A}$  in the presence of inhomogeneous coupling strength (solid red line). For comparison, if all atoms have the same coupling strength, this probability is simply given by  $p_{\text{exc}} = \sin(\bar{A}/2)^2$  (dashed blue line). For small mean pulse areas  $\bar{A}$ , the excitation probability is nearly the same with and without inhomogeneous broadening. However, deviations become apparent at larger  $\bar{A}$ . For example, in the presence of broadening, the maximum of  $p_{\text{exc}}$  occurs already at  $\bar{A} \approx 0.9\pi$  instead of at  $\pi$ . Moreover, the value of  $p_{\text{exc}}$  reaches, at most, about 0.8 in the presence of broadening.

In Fig. 7(b), we show the predictions for the imaginary part of the mean dipole moment  $d$  upon excitation, taking into account the averaging over the  $p(\beta_f)$  distribution.

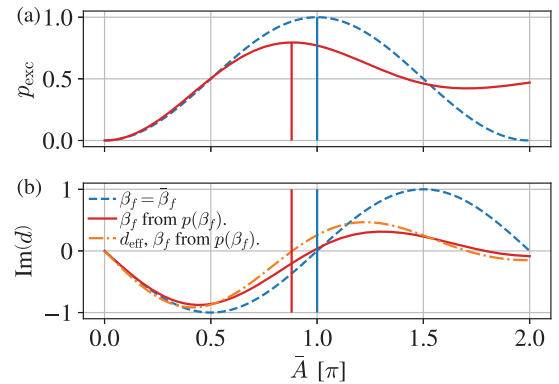


FIG. 7. Calculated excited state probability  $p_{\text{exc}}$  (a) and imaginary part of the dipole moment  $\text{Im}(d)$  (b) of a single atom when exposed to an infinitely short excitation pulse with varying mean pulse area  $\bar{A}$ . The blue dashed lines show the prediction for a fixed coupling strength  $\beta_f$ . The red solid lines take into account the distribution of  $\beta_f$  values. In (b) we also show an effective dipole moment  $\bar{d}_{\text{eff}}$  weighted by the factor  $\sqrt{\beta_f}/\langle\sqrt{\beta_f}\rangle$ . This effective dipole moment determines the optical field that the atom emits into the nanofiber-guided mode.

Here, we calculate the dipole moment in units of the transition dipole moment, such that  $d = 2\langle\hat{\sigma}\rangle$ . Similar to the case for  $p_{\text{exc}}$ , the deviation between the predictions for  $d$  with (solid red line) and without (blue dashed line) inhomogeneous distribution of  $\beta_f$  grows as  $\bar{A}$  increases.

Since we perform resonant excitation, the real part of the dipole moment vanishes. For a constant  $\beta_f$ , we simply have  $d = -i\sin(A)$ , and the zero crossing of  $\text{Im}(d)$  coincides with the point of maximal inversion at  $A = \pi$ , cf. vertical solid blue lines in Figs. 7(a) and 7(b). For a distribution of  $\beta_f$  values, the mean dipole moment is given by

$$d = -i\langle\sin[A(\beta_f)]\rangle. \quad (\text{A18})$$

In this case, zero mean dipole moment occurs at a slightly larger value of  $\bar{A}$  than the one at which  $p_{\text{exc}}$  is maximized. The relevant quantity for our burst experiments, however, is the field that an atom radiates into the waveguide, which is proportional to  $\sqrt{\beta_f}d$ . We thus define an effective mean dipole moment  $d_{\text{eff}}$  for which dipoles are weighted by  $\sqrt{\beta_f}$  in the averaging process,

$$d_{\text{eff}} = -i\left\langle\frac{\sqrt{\beta_f}}{\langle\sqrt{\beta_f}\rangle}\sin[A(\beta_f)]\right\rangle; \quad (\text{A19})$$

see orange dash-dotted line in Fig. 7(b). The zero crossing of  $\text{Im}(d_{\text{eff}})$  coincides with the point of maximal inversion (red vertical line). Thus, when  $\bar{A}$  is chosen so that  $p_{\text{exc}}$  is maximized, the field emitted by the atom features a vanishing expectation value; i.e., its phase is undefined.

### b. Cascaded excitation of an atomic ensemble

Since we excite the atomic ensemble through the nanofiber-guided mode in our experiment, each atom absorbs a part of the energy of the excitation pulse. Consequently, the pulse area seen by each atom decreases along the ensemble. In general, the problem is even more complicated because the pulse area present at each atom along the ensemble depends on the dynamics and the radiated light of all upstream atoms, as captured in the mixed coherent state model.

A simple way to parametrize the dynamics of the pulsed excitation of many atoms along the fiber is to specify the mean pulse area seen by the first atom in the row  $\bar{A}$ . In this case, given the absorption of the excitation pulse along the nanofiber-trapped ensemble, the ensemble-averaged excitation probability is maximized for a value of  $\bar{A}$  larger than that required for a single atom. In Fig. 8, we show the pulse area  $\bar{A}_{\text{max}}$  that maximally inverts an ensemble of  $N$  atoms. We show the simulation results for a fixed  $\beta_f$  as a blue dashed line and the results of the simulation taking into account a distribution of  $\beta_f$  values as a red solid line. Both these data show a linear increase, with a similar slope. Note that even for homogeneous coupling, a single atom is

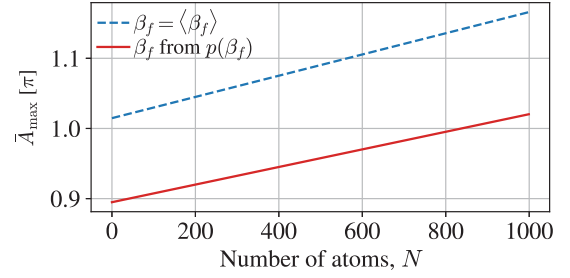


FIG. 8. Mean pulse area  $\bar{A}_{\text{max}}$  seen by the first atom ensuring that an ensemble of in total  $N$  atoms along the nanofiber is maximally inverted. We show the simulation results for fixed  $\beta_f$  (blue dashed line) and the results for a distribution of  $\beta_f$  values (red solid line). For the latter, we average over 500 randomly drawn  $\beta_f$  configurations and simulate a 4-ns-long excitation pulse. Because of absorption of the excitation pulse along the ensemble, the pulse area  $\bar{A}_{\text{max}}$  needed for maximal inversion increases for larger ensembles.

maximally inverted for  $\bar{A}_{\text{max}} \approx 1.02\pi$  because here we also take into account the finite pulse duration of 4 ns as used in the experiment.

Interestingly, in the presence of inhomogeneous coupling, for  $N \simeq 1000$ ,  $\bar{A}_{\text{max}} \approx \pi$ . This can be understood by considering the following. First, a single atom is on average maximally excited for a pulse area clearly smaller than  $\pi$  given an inhomogeneous distribution of coupling strengths, cf. Fig. 7. Second, the pulse area seen by each atom decreases along the ensemble due to absorption of the excitation pulse, such that one needs a larger pulse area to maximally excite an ensemble of atoms than a single atom. Since both effects are of a similar magnitude but feature opposite sign, the pulse area required to invert the about 1000 atoms in our experiment turns out to be very close to  $\pi$ .

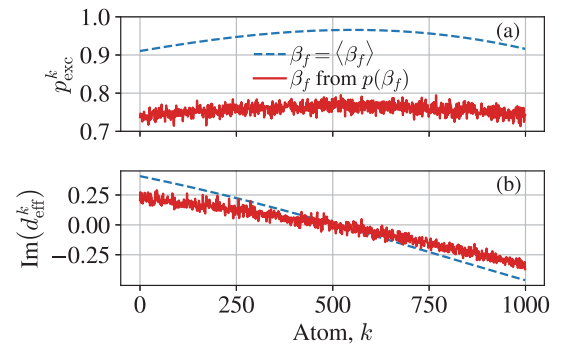


FIG. 9. Mean excited state probability (a) and imaginary part of the effective dipole moment (b) of the  $k$ th atom where we choose the pulse area  $\bar{A} = \bar{A}_{\text{max}}$  such that the atomic ensemble is maximally excited. We compute the density matrix of each atom after a 4-ns-long excitation pulse. We show the simulation results for a fixed  $\beta_f$  (blue dashed line) and for a distribution of  $\beta_f$  values (red solid line). For the latter, we average over 500 randomly drawn  $\beta_f$  configurations.

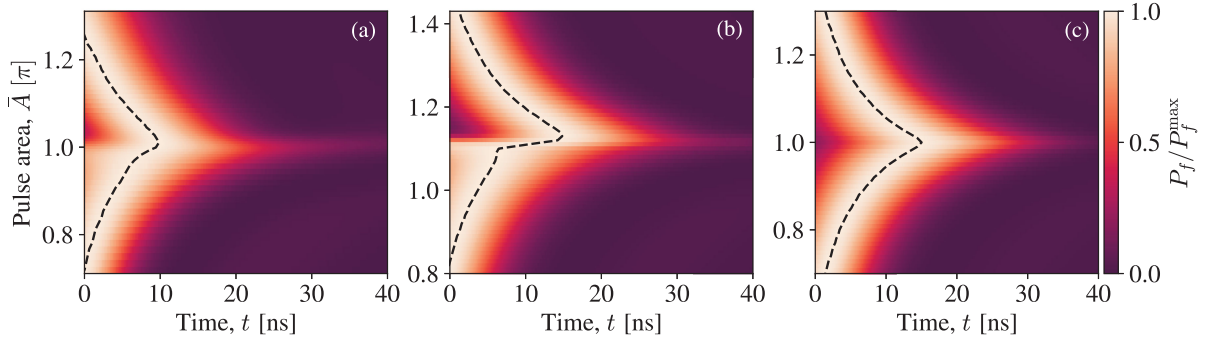


FIG. 10. Comparison of different model predictions for the dynamics of the power emitted into the forward-propagating mode  $P_f$  as a function of the pulse area seen by the first atom  $\bar{A}$ . Each time trace is normalized by its peak value  $P_f^{\max}$ . In (a) we assume inhomogeneous coupling strengths, absorption of the pulse during its propagation through the ensemble, and a 4-ns-long excitation pulse. (b) Same as in (a), except now assuming the same coupling strength for all atoms; i.e.,  $p(\beta_f)$  is a Delta function. In (c) we assume the same coupling strength for all atoms and perfect preparation of each atom in the initial state  $|\psi\rangle_{\text{ideal}}$ .

In Fig. 9(a), we show the mean excited state probability of the  $k$ th atom where we choose the pulse area  $\bar{A} = \bar{A}_{\max}$  such that an ensemble of 1000 atoms is maximally excited. Both for fixed  $\beta_f$  (blue dashed line) and for a distribution of  $\beta_f$  values (red solid line), the excitation probability is relatively uniform across the ensemble. In Fig. 9(b), we show the imaginary part of the effective dipole moment of the  $k$ th atom. In first approximation, we observe a linear decrease of  $\text{Im}(d_{\text{eff}})$  along the ensemble with a zero crossing occurring in the center. This dependence is expected since the first atoms are excited with a pulse area slightly larger than  $\pi$ , while the last atoms are excited with a pulse area slightly smaller than  $\pi$ .

### c. Influence on the collective dynamics

In order to study the influence of these imperfections on the collective dynamics, we compare different model predictions for the dynamics of the power emitted into the

forward direction  $P_f$  as a function of pulse area  $\bar{A}$ . Figure 10 shows the model predictions for 1000 atoms for three different assumptions. In Fig. 10(a), we include the temperature-induced fluctuations of the coupling strengths, the finite excitation pulse duration of 4 ns, and the absorption of the pulse during the propagation through the ensemble. This is the model prediction which we also show in the main text. In Fig. 10(b), we assume the same as in Fig. 10(a) except that all atoms now have the same coupling strength. Qualitatively, the dynamics is still similar to the one displayed in Fig. 10(a). However, the asymmetry with respect to the point of maximal excitation is more pronounced in Fig. 10(b), and the maximal delay is larger. The asymmetry of the time traces with respect to maximal excitation is due to a combination of the pulse absorption along the ensemble and the fact that we work with a cascaded system. There, the first atom will always emit independently, while the last atom is driven by the light emitted by the entire ensemble. For a pulse area  $\bar{A}$

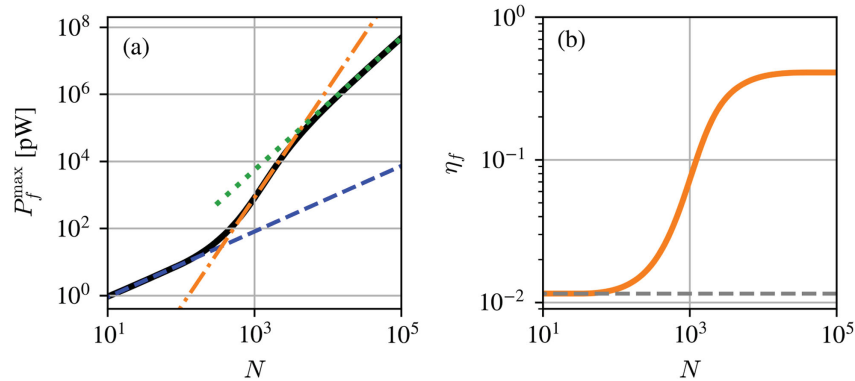


FIG. 11. Model predictions for the scaling of different quantifiers of the superradiant burst with the number of atoms  $N$ . We assume a homogeneous atom-waveguide coupling strength of  $\beta_f = 0.011$  and perfect inversion at time  $t = 0$  ns. (a) We observe three regimes, in which the predicted value of  $P_f^{\max}$  scales linearly (blue dashed line), superquadratically (orange dash-dotted line), and quadratically (green dotted line) with  $N$ . (b) The predicted collective coupling efficiency  $\eta_f$  is constant and has a value of  $\approx \beta_f$  for small values of  $N$ . In the intermediate- $N$  regime,  $\eta_f$  grows with  $N$ . For large  $N$ ,  $\eta_f$  reaches a constant value.

slightly larger than  $\pi$ , the last atom is prepared closer to full inversion than the first atom, and, consequently, the superradiant burst is more pronounced than for a pulse area  $\bar{A}$  slightly smaller than  $\pi$ . In Fig. 10(c), we assume that all atoms are initially prepared in  $|\psi\rangle_{\text{ideal}}$  and that all atoms feature the same coupling strength to the nanofiber-guided mode. In this case, the emission dynamics is symmetric with respect to  $\bar{A} = \pi$ .

### 7. Scaling in the large- $N$ limit

We now investigate the scaling of the superradiant burst for larger  $N$  and simulate the dynamics of up to  $10^5$  atoms. To do so, we assume a homogeneous coupling strength of  $\beta_f = 0.011$  as well as perfect inversion at time  $t = 0$ . In Fig. 11(a), we plot the predicted peak power  $P_f^{\text{max}}$  as a function of  $N$  (black line). We observe three different regimes of scaling. For small atom numbers,  $P_f^{\text{max}}$  scales linearly with  $N$  (blue dashed line). Above the threshold atom number for the occurrence of a superradiant burst, the scaling becomes faster than quadratic, which corresponds to the observation in our experiment. For atom numbers between 500 and 2000, we extract a power-law exponent of 3.25 from the fit (orange dash-dotted line). We numerically checked that the difference to the experimentally observed exponent of 2.6(2) is mainly due to the inhomogeneous spread of coupling strengths  $\beta_f$ . Eventually, the scaling becomes quadratic for even larger  $N$  (green dotted line). This is expected in the limit of large  $N$ , because we attribute the superquadratic scaling of  $P_f^{\text{max}}$  to an increase of the collective coupling efficiency  $\eta_f$ , and  $\eta_f$  is bounded at 1. In Fig. 11(b), we plot  $\eta_f$  as a function of  $N$  and indeed observe that  $\eta_f$  approaches a constant value for large  $N$ . Based on our model prediction,  $\eta_f \approx 0.4$  for  $N \simeq 10^5$  atoms. However, we note that the mixed coherent state model used for the simulations has not been benchmarked with experimental data for such a large number of atoms.

---

[1] S. Haroche and J.-M. Raimond, *Exploring the Quantum: Atoms, Cavities, and Photons* (Oxford University Press, Oxford, 2006).

[2] P. Lodahl, S. Mahmoodian, S. Stobbe, A. Rauschenbeutel, P. Schneeweiss, J. Volz, H. Pichler, and P. Zoller, *Chiral quantum optics*, *Nature (London)* **541**, 473 (2017).

[3] C. Sayrin, C. Junge, R. Mitsch, B. Albrecht, D. O'Shea, P. Schneeweiss, J. Volz, and A. Rauschenbeutel, *Nanophotonic optical isolator controlled by the internal state of cold atoms*, *Phys. Rev. X* **5**, 041036 (2015).

[4] S. Mahmoodian, P. Lodahl, and A. S. Sørensen, *Quantum networks with chiral-light-matter interaction in waveguides*, *Phys. Rev. Lett.* **117**, 240501 (2016).

[5] O. Bechler, A. Borne, S. Rosenblum, G. Guendelman, O.E. Mor, M. Netser, T. Ohana, Z. Aqua, N. Drucker,

R. Finkelstein *et al.*, *A passive photon-atom qubit swap operation*, *Nat. Phys.* **14**, 996 (2018).

[6] C. W. Gardiner, *Driving a quantum system with the output field from another driven quantum system*, *Phys. Rev. Lett.* **70**, 2269 (1993).

[7] H. J. Carmichael, *Quantum trajectory theory for cascaded open systems*, *Phys. Rev. Lett.* **70**, 2273 (1993).

[8] R. H. Dicke, *Coherence in spontaneous radiation processes*, *Phys. Rev.* **93**, 99 (1954).

[9] M. Gross and S. Haroche, *Superradiance: An essay on the theory of collective spontaneous emission*, *Phys. Rep.* **93**, 301 (1982).

[10] N. Skribanowitz, I. Herman, J. MacGillivray, and M. Feld, *Observation of Dicke superradiance in optically pumped HF gas*, *Phys. Rev. Lett.* **30**, 309 (1973).

[11] M. Gross, C. Fabre, P. Pillet, and S. Haroche, *Observation of near-infrared Dicke superradiance on cascading transitions in atomic sodium*, *Phys. Rev. Lett.* **36**, 1035 (1976).

[12] M. Gross, P. Goy, C. Fabre, S. Haroche, and J. M. Raimond, *Maser oscillation and microwave superradiance in small systems of Rydberg atoms*, *Phys. Rev. Lett.* **43**, 343 (1979).

[13] J. G. Bohnet, Z. Chen, J. M. Weiner, D. Meiser, M. J. Holland, and J. K. Thompson, *A steady-state superradiant laser with less than one intracavity photon*, *Nature (London)* **484**, 78 (2012).

[14] A. Goban, K. S. Choi, D. J. Alton, D. Ding, C. Lacroûte, M. Pototschnig, T. Thiele, N. P. Stern, and H. J. Kimble, *Demonstration of a state-insensitive, compensated nanofiber trap*, *Phys. Rev. Lett.* **109**, 033603 (2012).

[15] M. A. Norcia, M. N. Winchester, J. R. Cline, and J. K. Thompson, *Superradiance on the millihertz linewidth strontium clock transition*, *Sci. Adv.* **2**, e1601231 (2016).

[16] G. Ferioli, A. Glicenstein, F. Robicheaux, R. T. Sutherland, A. Browaeys, and I. Ferrier-Barbut, *Laser-driven superradiant ensembles of two-level atoms near Dicke regime*, *Phys. Rev. Lett.* **127**, 243602 (2021).

[17] L. Ostermann, H. Zoubi, and H. Ritsch, *Cascaded collective decay in regular arrays of cold trapped atoms*, *Opt. Express* **20**, 29634 (2012).

[18] S. J. Masson, I. Ferrier-Barbut, L. A. Orozco, A. Browaeys, and A. Asenjo-Garcia, *Many-body signatures of collective decay in atomic chains*, *Phys. Rev. Lett.* **125**, 263601 (2020).

[19] S. J. Masson and A. Asenjo-Garcia, *Universality of Dicke superradiance in arrays of quantum emitters*, *Nat. Commun.* **13**, 2285 (2022).

[20] E. Sierra, S. J. Masson, and A. Asenjo-Garcia, *Dicke superradiance in ordered lattices: Dimensionality matters*, *Phys. Rev. Res.* **4**, 023207 (2022).

[21] F. Robicheaux, *Theoretical study of early-time superradiance for atom clouds and arrays*, *Phys. Rev. A* **104**, 063706 (2021).

[22] O. Rubies-Bigorda and S. F. Yelin, *Superradiance and subradiance in inverted atomic arrays*, *Phys. Rev. A* **106**, 053717 (2022).

[23] B. Lemberger and K. Mølmer, *Radiation eigenmodes of Dicke superradiance*, *Phys. Rev. A* **103**, 033713 (2021).

[24] D. Plankensteiner, C. Hotter, and H. Ritsch, *QuantumCumulants.jl: A Julia framework for generalized mean-field*

- equations in open quantum systems*, *Quantum* **6**, 617 (2022).
- [25] F. T. Arecchi, E. Courtens, R. Gilmore, and H. Thomas, *Atomic coherent states in quantum optics*, *Phys. Rev. A* **6**, 2211 (1972).
- [26] K. Stannigel, P. Rabl, and P. Zoller, *Driven-dissipative preparation of entangled states in cascaded quantum-optical networks*, *New J. Phys.* **14**, 063014 (2012).
- [27] H. Pichler, T. Ramos, A. J. Daley, and P. Zoller, *Quantum optics of chiral spin networks*, *Phys. Rev. A* **91**, 042116 (2015).
- [28] J. Kumlin, K. Kleinbeck, N. Stiesdal, H. Busche, S. Hofferberth, and H. P. Büchler, *Nonexponential decay of a collective excitation in an atomic ensemble coupled to a one-dimensional waveguide*, *Phys. Rev. A* **102**, 063703 (2020).
- [29] S. Cardenas-Lopez, S. J. Masson, Z. Zager, and A. Asenjo-Garcia, *Many-body superradiance and dynamical mirror symmetry breaking in waveguide QED*, *Phys. Rev. Lett.* **131**, 033605 (2023).
- [30] A. S. Sheremet, M. I. Petrov, I. V. Iorsh, A. V. Poshakinskiy, and A. N. Poddubny, *Waveguide quantum electrodynamics: Collective radiance and photon-photon correlations*, *Rev. Mod. Phys.* **95**, 015002 (2023).
- [31] E. Vetsch, D. Reitz, G. Sagué, R. Schmidt, S. T. Dawkins, and A. Rauschenbeutel, *Optical interface created by laser-cooled atoms trapped in the evanescent field surrounding an optical nanofiber*, *Phys. Rev. Lett.* **104**, 203603 (2010).
- [32] N. Schlosser, G. Reymond, and P. Grangier, *Collisional blockade in microscopic optical dipole traps*, *Phys. Rev. Lett.* **89**, 023005 (2002).
- [33] E. Vetsch, S. T. Dawkins, R. Mitsch, D. Reitz, P. Schneeweiss, and A. Rauschenbeutel, *Nanofiber-based optical trapping of cold neutral atoms*, *IEEE J. Sel. Top. Quantum Electron.* **18**, 1763 (2012).
- [34] Y. Meng, A. Dureau, P. Schneeweiss, and A. Rauschenbeutel, *Near-ground-state cooling of atoms optically trapped 300 nm away from a hot surface*, *Phys. Rev. X* **8**, 031054 (2018).
- [35] D. A. Steck, *Alkali D line data*, <https://steck.us/alkalidata>.
- [36] F. L. Kien, J. Liang, K. Hakuta, and V. Balykin, *Field intensity distributions and polarization orientations in a vacuum-clad subwavelength-diameter optical fiber*, *Opt. Commun.* **242**, 445 (2004).
- [37] R. Mitsch, C. Sayrin, B. Albrecht, P. Schneeweiss, and A. Rauschenbeutel, *Quantum state-controlled directional spontaneous emission of photons into a nanophotonic waveguide*, *Nat. Commun.* **5**, 5713 (2014).
- [38] C. Liedl, S. Pucher, F. Tebbenjohanns, P. Schneeweiss, and A. Rauschenbeutel, *Collective radiation of a cascaded quantum system: From timed Dicke states to inverted ensembles*, *Phys. Rev. Lett.* **130**, 163602 (2023).
- [39] A. Tiranov, V. Angelopoulou, C. J. van Diepen, B. Schirnski, O. A. D. Sandberg, Y. Wang, L. Midolo, S. Scholz, A. D. Wieck, A. Ludwig, A. S. Sørensen, and P. Lodahl, *Collective super- and subradiant dynamics between distant optical quantum emitters*, *Science* **379**, 389 (2023).
- [40] P. Solano, P. Barberis-Blostein, F. K. Fatemi, L. A. Orozco, and S. L. Rolston, *Super-radiance reveals infinite-range dipole interactions through a nanofiber*, *Nat. Commun.* **8**, 1857 (2017).
- [41] N. V. Corzo, J. Raskop, A. Chandra, A. S. Sheremet, B. Gouraud, and J. Laurat, *Waveguide-coupled single collective excitation of atomic arrays*, *Nature (London)* **566**, 359 (2019).
- [42] S. Okaba, D. Yu, L. Vincetti, F. Benabid, and H. Katori, *Superradiance from lattice-confined atoms inside hollow core fibre*, *Commun. Phys.* **2**, 136 (2019).
- [43] R. Pennetta, D. Lechner, M. Blaha, A. Rauschenbeutel, P. Schneeweiss, and J. Volz, *Observation of coherent coupling between super- and subradiant states of an ensemble of cold atoms collectively coupled to a single propagating optical mode*, *Phys. Rev. Lett.* **128**, 203601 (2022).
- [44] R. Loudon, *The Quantum Theory of Light*, 3rd ed. (Oxford University Press, Oxford, 2000).
- [45] R. Bonifacio and L. Lugiato, *Cooperative radiation processes in two-level systems: Superfluorescence*, *Phys. Rev. A* **11**, 1507 (1975).
- [46] C. Fabre and N. Treps, *Modes and states in quantum optics*, *Rev. Mod. Phys.* **92**, 035005 (2020).
- [47] M. Perarnau-Llobet, A. González-Tudela, and J. I. Cirac, *Multimode Fock states with large photon number: Effective descriptions and applications in quantum metrology*, *Quantum Sci. Technol.* **5**, 025003 (2020).
- [48] H. J. Carmichael, *Spectrum of squeezing and photocurrent shot noise: A normally ordered treatment*, *J. Opt. Soc. Am. B* **4**, 1588 (1987).
- [49] R. J. Glauber, *The quantum theory of optical coherence*, *Phys. Rev.* **130**, 2529 (1963).
- [50] H. M. Wiseman and G. J. Milburn, *Quantum theory of field-quadrature measurements*, *Phys. Rev. A* **47**, 642 (1993).
- [51] H. M. Wiseman and G. J. Milburn, *Quantum Measurement and Control* (Cambridge University Press, Cambridge, England, 2009).
- [52] A. Bolund and K. Mølmer, *Stochastic excitation during the decay of a two-level emitter subject to homodyne and heterodyne detection*, *Phys. Rev. A* **89**, 023827 (2014).
- [53] F. L. Kien and K. Hakuta, *Cooperative enhancement of channeling of emission from atoms into a nanofiber*, *Phys. Rev. A* **77**, 013801 (2008).
- [54] S. Mahmoodian, G. Calajó, D. E. Chang, K. Hammerer, and A. S. Sørensen, *Dynamics of many-body photon bound states in chiral waveguide QED*, *Phys. Rev. X* **10**, 031011 (2020).
- [55] C. W. Gardiner and M. J. Collett, *Input and output in damped quantum systems: Quantum stochastic differential equations and the master equation*, *Phys. Rev. A* **31**, 3761 (1985).
- [56] L. Mandel and E. Wolf, *Optical Coherence and Quantum Optics* (Cambridge University Press, Cambridge, England, 1995).
- [57] K. J. Kusmierek, S. Mahmoodian, M. Cordier, J. Hinney, A. Rauschenbeutel, M. Schemmer, P. Schneeweiss, J. Volz, and K. Hammerer, *Higher-order mean-field theory of chiral waveguide QED*, *SciPost Phys. Core* **6**, 041 (2023).
- [58] V. Paulisch, M. Perarnau-Llobet, A. González-Tudela, and J. I. Cirac, *Quantum metrology with one-dimensional super-radiant photonic states*, *Phys. Rev. A* **99**, 043807 (2019).
- [59] A. González-Tudela, V. Paulisch, D. E. Chang, H. J. Kimble, and J. I. Cirac, *Deterministic generation of*

- arbitrary photonic states assisted by dissipation*, *Phys. Rev. Lett.* **115**, 163603 (2015).
- [60] O. Tziperman, G. Baranes, A. Gorlach, R. Ruimy, M. Faran, N. Gutman, A. Pizzi, and I. Kaminer, *Spontaneous emission from correlated emitters*, [arXiv:2306.11348](https://arxiv.org/abs/2306.11348).
- [61] F. Jahnke, C. Gies, M. Abmann, M. Bayer, H. Leymann, A. Foerster, J. Wiersig, C. Schneider, M. Kamp, and S. Höfling, *Giant photon bunching, superradiant pulse emission and excitation trapping in quantum-dot nanolasers*, *Nat. Commun.* **7**, 11540 (2016).
- [62] G. Ferioli, A. Glicenstein, I. Ferrier-Barbut, and A. Browaeys, *A non-equilibrium superradiant phase transition in free space*, *Nat. Phys.* **19**, 1345 (2023).
- [63] T. Ramos, H. Pichler, A. J. Daley, and P. Zoller, *Quantum spin dimers from chiral dissipation in cold-atom chains*, *Phys. Rev. Lett.* **113**, 237203 (2014).
- [64] D. Meiser, J. Ye, D. R. Carlson, and M. J. Holland, *Prospects for a millihertz-linewidth laser*, *Phys. Rev. Lett.* **102**, 163601 (2009).
- [65] H. J. Carmichael, *Statistical Methods in Quantum Optics I: Master Equations and Fokker-Planck Equations*, Vol. 1 (Springer-Verlag Berlin Heidelberg, 1999).
- [66] B. Olmos, C. Liedl, I. Lesanovsky, and P. Schneeweiss, *Bragg condition for scattering into a guided optical mode*, *Phys. Rev. A* **104**, 043517 (2021).